https://doi.org/10.5194/egusphere-2025-6510
Preprint. Discussion started: 13 January 2026

Extraction of multiple ages from c-axis projected fission tracks

Peter K. Jensen[1]

[1]Department of Environmental and Resource Engineering, Technical University of Denmark, Kgs. Lyngby, 2800, Denmark

Correspondence to: Peter K. Jensen (pklje@dtu.dk)

Abstract. The traditional fission track age equation accurately calculates the cooling age for apatite minerals when the cooling rate is fast. Nevertheless, it is used when the cooling rate is gradual, for example when the age of transition through the partial annealing window is to be estimated. Added age information is here obtained by inclusion of the length distribution of fully included near horizontal tracks. The tendency that the shortest tracks are the oldest ones, and the longest ones are the youngest enables the age dating of a given track by counting the number of shorter tracks, adding one, and dividing by the volumetric track generation rate. The difficulty is that the track length–age relation is blurred by the spread in lengths due to crystallographic anisotropy and observational uncertainties. The blurring can be reduced by mathematical deconvolution in which the blurring of tracks in annealing experiments is used. Previously developed equations are updated to improve precision. This paper presents a method where deblurring is first performed by projecting the observed track lengths on the mineral c-axis and then by deblurring using probabilistic least squares inversion. This leads to the extraction of several track ages with deviations for each deconvolved track length histogram. This information may be used to constrain the timing of tectonic events and provide the basis for calculation of past temperature.

1 Fission track age equations

The traditional fission track age equation (Kohn et al., 2024) is used to calculate the age of rapid cooling apatite minerals to temperatures below 60 °C. For example, the age of volcanic extrusion on the surface is calculated with precision in this way. The essential parameters in the equation are the surface track density, the uranium concentration, and a calibration constant. The equation is also applied to obtain the apparent age for apatite minerals when cooling is gradual through the partial annealing window from 120 °C to 60 °C. However, this single age determination can only be regarded as a rough estimate. Jensen and Hansen (2021) showed that several ages can be derived by deconvolution of track length histograms of non- c-axis projected fully included near horizontal fission tracks.

In this paper the deconvolution method is further developed to apply to c-axis projected tracks. The theoretical foundation is the work by Bertagnolli et al. (1983) and Keil et al. (1987). The starting point is the randomly fully included oriented non-etched fission track in minerals caused by the natural fission of U-238. The tracks are generated through time, and the length is shortened as a function of time so that ideally the oldest tracks are the shortest ones and the more recent tracks are the

https://doi.org/10.5194/egusphere-2025-6510
Preprint. Discussion started: 13 January 2026

longest ones. A given track can therefore be aged by counting the number of shorter tracks, adding one, and dividing by the track generation rate. This is expressed in the equation (Keil et al., 1987):

$$\tau(\lambda_0) = \frac{1}{\varepsilon}\int_1^{\lambda_0} n(\lambda)d\lambda\,, \quad (1)$$

where $\tau(\lambda_0)$ is the age of a track with a normalized length λ_0, ε is the volumetric track generation rate (tracks/(sec. m^3), $n(\lambda)$ is the volumetric density (tracks/m^3) of tracks with normalized length λ. The integration is performed from the longest tracks (newest) $\lambda = 1$ to the shorter track (older) $\lambda = \lambda_0$. As seen from Eq. (1) there is no need for the surface track density and a track length annealing model to derive the age of a track. Unfortunately, it is difficult to see the randomly oriented tracks with a diameter of a few angstroms (Li et al., 2011). Instead, it is therefore practice making them visible in the light microscope by etching (Kohn et al., 2024). To enable length measurement only the near horizontal tracks with a connection to the surface are selected for length measurement. Uranium concentration is also needed. To estimate the ages of etched tracks a mathematical model relating etched tracks to unetched tracks is needed. Due to various biases and uncertainties (Ketcham, 2005) the observed track length histogram of etched tracks is blurred. This means that the relation between histogram columns and the time intervals in which they were generated is non-unique. Fortunately, the blurring is known from artificial annealing experiments and can, to some extent, be removed from the observed track length histogram by mathematical deconvolution (Jensen et al., 1992; Donelick et al., 1988). Probabilistic inversion (Tarantola, 2005) including prior information was implemented for non-c-axis projected tracks (Jensen and Hansen, 2021). The track length histograms were transformed to deconvolved histograms with a tighter relation between histogram columns and time intervals. The derived deblurred track length histogram was then converted to a time interval histogram. Cumulation of the time interval histogram from the most recent to the older time intervals provided the age of the oldest track of each histogram column, at least those being statistically significant. In this paper the deconvolution technique presented takes advantage of the c-axis projection method by Donelick et al. (1999). In this way there is a tendency that tracks generated in the same time intervals are brought together in the same histogram columns of c-axis projected tracks. But there is still blurring left which can be deblurred by deconvolution as described here. c-axis projected laboratory annealed tracks are used as the kernel. An approximation in the equations given in Jensen and Hansen (2021) is replaced by exact expressions. The inversion technique uses the method of least squares which does not exclude negative deconvolved histogram columns. This is of course unrealistic, but the problem can be resolved by the choice of positive priors with small variances but large enough to avoid the priors dominating the histograms. The mathematical derivations are given in Appendix A. And overview of symbols is shown in Appendix C. Applications are given in the next section.

2 Application of age nodes

Fission track data from Ellesmere Island and Northwest Greenland (Spiegel et al., 2023a; 2023b) are used to illustrate the calculation of age nodes. Calibrations are performed using the new equations with data sets of Uranium concentrations and surface track densities and a histogram of unannealed tracks and then compare with the corresponding apparent age with

https://doi.org/10.5194/egusphere-2025-6510
Preprint. Discussion started: 13 January 2026

deviation. The unannealed histogram is based on artificial tracks at 20 °C (Barbarand et al., 2003) and used after conversion to c-axis projected tracks. The resulting calibration constants are given in the Supplement, Table S1.

Calculation of age nodes for the Late Devonian sandstone sample CXII_46 (Fig. 1A) shows the measured c-axis projected fission track length histogram. It is seen that the deconvolved track length histogram (Fig. 1B) is condensed with respect to the track length compared to the original c-axis projected tracks (Fig. 1A). Deconvolution tends to collect the tracks generated in the same time intervals. The columns of the deconvolved track length histogram (Fig. 1B) are converted to equivalent time intervals (Fig. 1C) using Eq. (A18). The age of the oldest track in each column (Fig. 1C) is derived after cumulation from the longest to the shortest tracks. Three age nodes with non-overlapping deviations are found: 80 ±27 Ma, 271 ±40 Ma and 446 ±34 Ma, Table 1. The oldest track age, 446 ±34 Ma, is older than the deposition age of the Late Devonian sandstone (359-383 Ma). This means that the apatite minerals hold pre-sedimentary inherited tracks. The post-sedimentary columns of the deconvolved histogram (Fig. 1B) were found by identifying the columns with track ages less than the deposition age. In this case they are the three right most track length histogram columns. Post-sedimentary tracks are 85% of the total number of tracs.

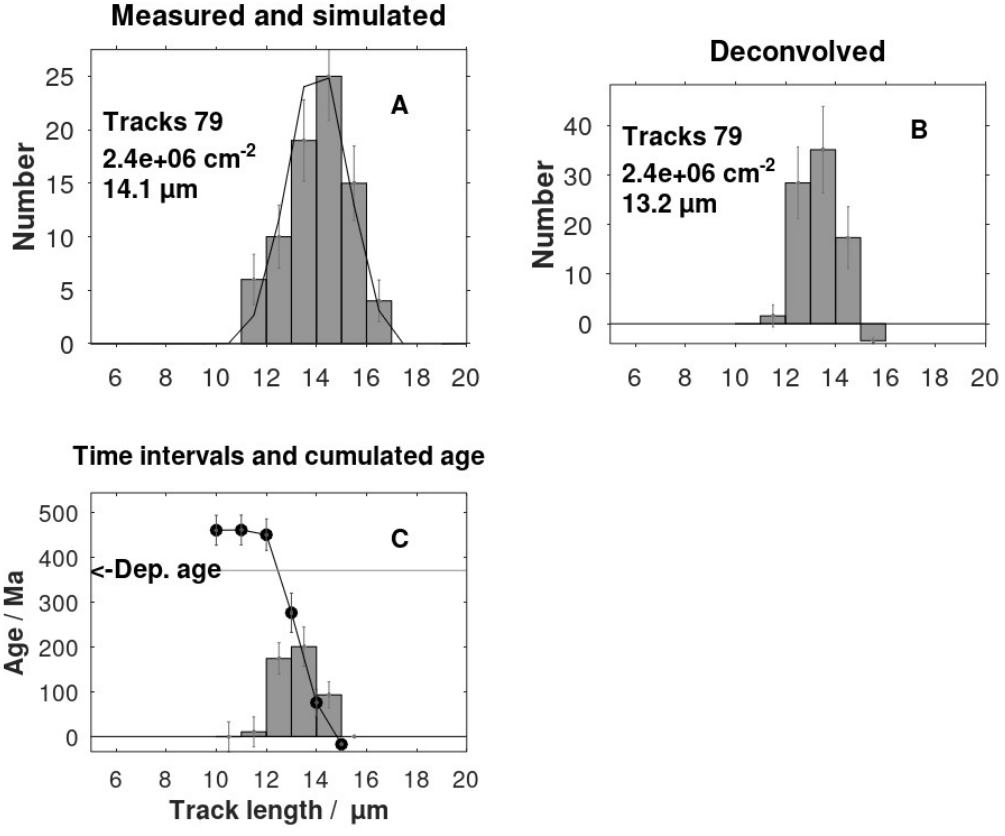

https://doi.org/10.5194/egusphere-2025-6510
Preprint. Discussion started: 13 January 2026

Figure 1: A. c-axis projected track histogram of a sandstone sample CXII-46, Spiegel et al., (2023b) together with distribution. B. Deconvolution of the histogram in a. C. Histogram of time intervals and cumulated track ages. The horizontal line shows the deposition age. D.

Table 1. Age nodes related to deconvolved track length, calibration factors, rock ages (Spiegel et al., 2023b), age of oldest track, fission track central ages (Spiegel et al., 2023b).

Sample Lithology	Rock age Oldest age Central age	Deconvolved track length	Age nodes	Calibration factor
	Ma	µm	Ma	
CXII-46 Sandstone	359-383 458 (33) 386 (28)	14 13 12	76 (25) 277 (44) 451 (35)	1.66
GRÖ21 Gneiss	2500-4000 125 (10) 99 (9)	13 12 11	43 (9) 79 (11) 125 (10)	1.02
GRÖ64 Gneiss	2500-4000 206 (16) 160 (11)	13 11	81 (17) 204 (16)	1.004

Deconvolution tends to enhance bimodality as seen by comparing Fig. 2A and 2B for sample GRÖ64 (Spiegel et al., 2023b). The age of the oldest track is 193 (16) Ma. The bimodality indicates the presence of three levels of maximum temperature: 1) a long period (193-95 Ma) in which the maximum temperature reached the upper part of the partial annealing window (120 °C to 60 °C) followed by 2) a shorter cooling period (95-66 Ma) where the maximum temperature reached the lower part of the partial annealing window followed by 3) a long period of moderate temperatures below 60 °C until the present.

.

https://doi.org/10.5194/egusphere-2025-6510
Preprint. Discussion started: 13 January 2026

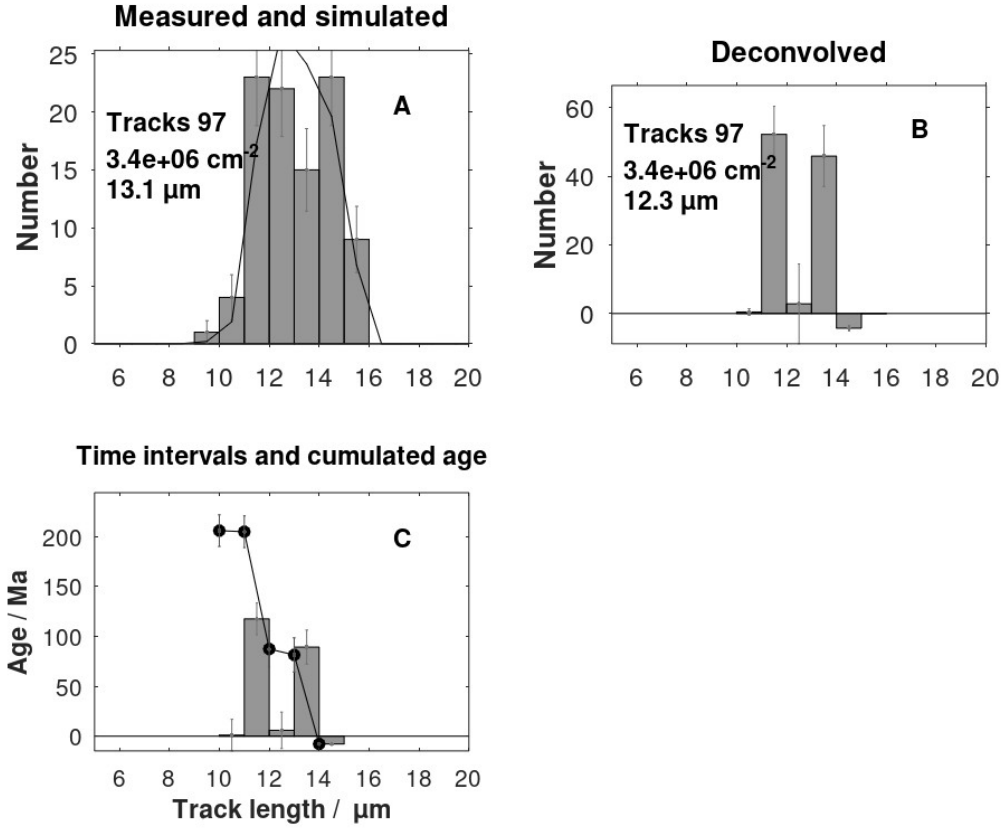

Figure 2: A. c-axis projected track histogram for sample GRÖ64 (Spiegel et al., 2023b) and the calculated distribution. B. Deconvolution of the c-axis projected tracks. C. Histogram of time intervals and cumulated track ages.

The last example (Fig. 3) shows the enhancement of bimodality after the deconvolution of the tracks for sample GRÖ21 (Spiegel et al., 2023b). The measured c-axis projected histogram is broad but non-bimodal. In contrast, the deconvolved histogram shows bimodality.

https://doi.org/10.5194/egusphere-2025-6510
Preprint. Discussion started: 13 January 2026

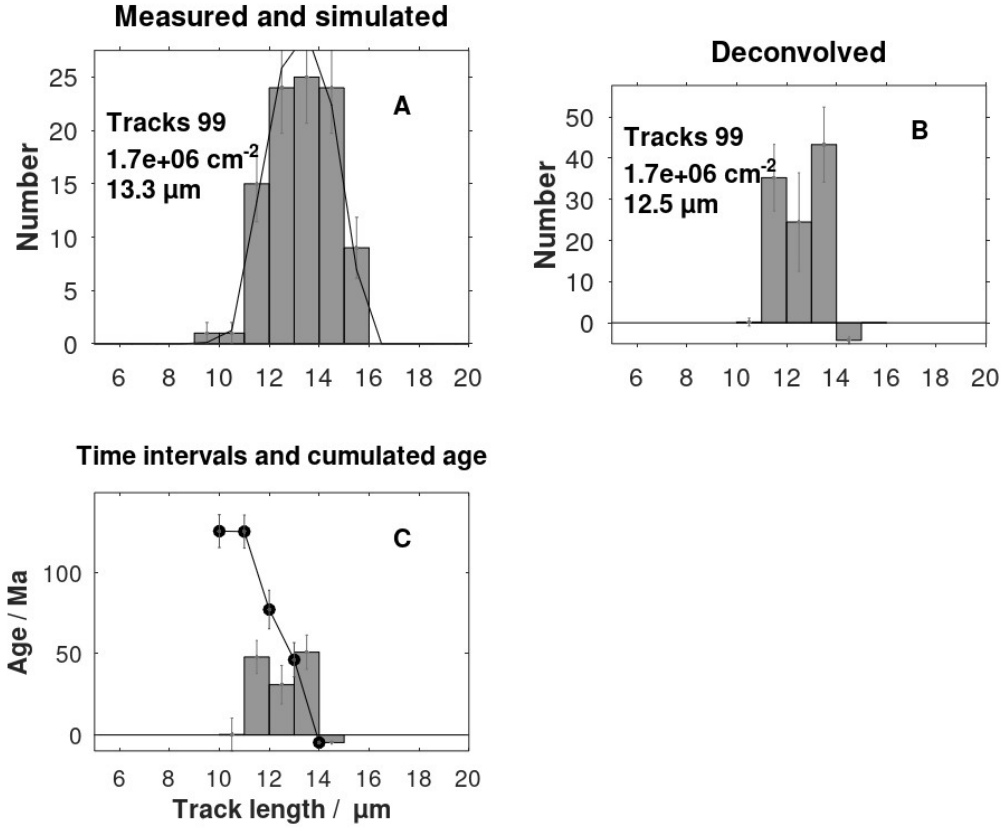

Figure 3: A. c-axis projected track histogram of the gneiss sample GRÖ21 (Spiegel et al. 2023b) and the calculated distribution. B. Deconvolution. C. Histogram of time intervals and cumulated track ages.

Table S1 (Supplement) shows the calculated age nodes related to the deconvolved track lengths for several samples given by Spiegel et al. (2023b). The computer program written in Octave (Eaton et al., 2020) calculates the oldest track age for each column of the time interval histogram, but only ages with deviations that are not overlapping nearby age deviations are regarded as reliable age nodes. The number of reliable age nodes given in Table S1 is from two to five with three in mean. Central ages (Spiegel et al., 2023a) as a function of the calculated oldest ages (this study) show that most central ages are 20% lower than the oldest ages, Fig. 4. The oldest ages are close to the ages of the last peak temperatures above 100 °C (Spiegel et al., 2023b), however with large deviations.

https://doi.org/10.5194/egusphere-2025-6510
Preprint. Discussion started: 13 January 2026

110

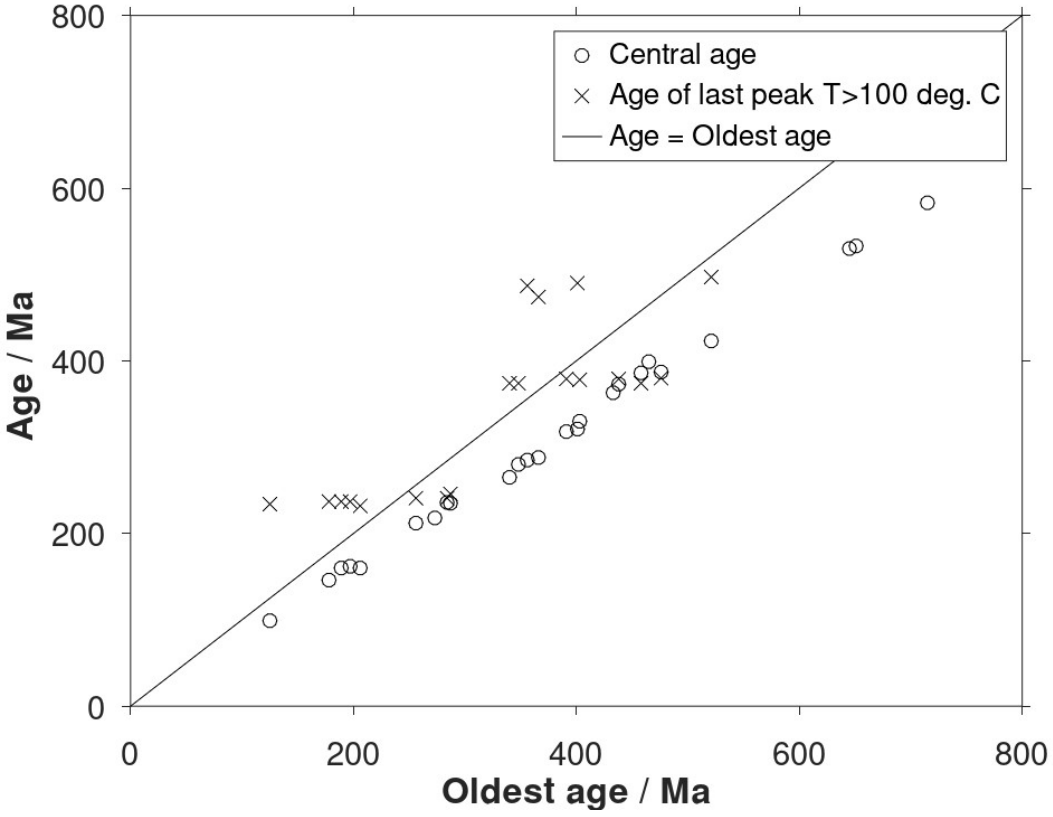

Figure 4: Simulated ages by HeFTy of the last temperature peak with temperatures above 100 °C and central apparent ages (Spiegel et al., 2023b) as a function of the oldest age.

115 **3 Discussion**

The least squares inversion method allows negative posterior values (negative histogram columns) which is physically unrealistic. The problem occurs when the physical model is inadequate and the data are mistaken. It is solved by restricting the posterior track length window and choosing positive priors with variances small enough to ensure mainly positive posteriors, but on the other hand so large that the priors do not dominate over the data. The inversion set up applied here
120 assumes the track length histogram columns to be normally distributed. A better distribution is Poisson's distribution. Fortunately, the normal distribution is a reasonable approximation for columns of more than five tracks (Bardsley, 2018). In

https://doi.org/10.5194/egusphere-2025-6510
Preprint. Discussion started: 13 January 2026

the future, the generalized normal distribution or the log-normal distribution (Tarantola, 2005) may be considered to avoid negative columns. The selection of the normal distribution offers simple equations and direct calculations instead of Monte Carlo type simulations with ten thousand realizations (Gallagher, 2012; Ketcham, 2019). Inversion of matrices like those in Eq. (A24) and (A25) may be non-stable. The stability is tested by calculating the condition numbers for matrixes that are to be inverted. In this case the numbers are small, showing numerical stability. Cholesky factorization is therefore not necessary (Calvetti and Somersalo, 2007).

4 Conclusion

Equations used to calculate multiple age nodes with deviations for apatite fission track length histograms are updated. The equations are based on probabilistic least squares inversion that mitigates the blurring of measured track length histograms. Prior model values are chosen to minimize time-intervals with negative values. The equations were implemented in a computer program (Octave, Eaton et al., 2020) and tested using c-axis projected track data from the Canadian Precambrian Shield. The c-axis projection of the tracks and prior values stabilizes the inversion. Ages of the oldest tracks show conformity with ages of the last temperature peaks above 100 ° C, however with large deviations. The ages of the oldest tracks are in the mean 20% older than the reported central ages. The age variance shows that two to five age estimates are realistic for c-axis projected track histograms. Moderate bimodality of histograms is enhanced by the deconvolution, promoting the age date estimation of tectonic events. Multiple age node estimates may guide the selection of the age-temperature boxes applied in fission track simulation models.

Appendix A

Jensen and Hansen (2021) discussed direct calculation of multiple age nodes for individual fission track length histograms for non-c-axis projected tracks. The equations are here updated for the use of c-axis projected tracks, which are commonly reported in fission track studies. To deconvolve c-axis projected track histograms, laboratory annealed fission track data are needed. They are derived from laboratory annealing experiments (Barbarand et al., 2003 and Ravenhurst et al., 2003) and are then c-axis projected following Donelick et al. (1999). The approximation used to derive Eq. (38) in Jensen and Hansen (2021) is here replaced by an exact expression leading to updated equations.

In a short time-interval Δt^i the natural fission of U-238 initially generates a number n^i of randomly oriented tracks in the mineral:

$$n^i = \lambda_f c \Delta t^i \quad \text{for } i = 1 \dots N, \tag{A1}$$

where λ_f is the fission decay frequency, c is the U–238 concentration, i numbers the time intervals from the oldest to the most recent interval. Due to the energy dispersion of fission fragments (Jungerman and Wright, 1949), the initial spread of track lengths forms a track length histogram:

$$\boldsymbol{n}^i = (n_1^i \dots n_j^i \dots n_M^i)^T, \tag{A2}$$

https://doi.org/10.5194/egusphere-2025-6510
Preprint. Discussion started: 13 January 2026

where j numbers the track length binning from the shortest to the longest tracks. ^{T} indicates mathematical transposition.

The initial tracks shorten due to time and the temperature of the mineral. The tracks are further spread in length because of the various orientations relative to the crystal axes. The modified random oriented track length histogram with origin in the time-interval i is

$$\boldsymbol{v}^i = (v_1^i \dots v_j^i \dots v_M^i)^T. \quad \text{(A3)}$$

Consider the time-interval Δt^i that produced a number of, not totally annealed, tracks. The total number of these randomly oriented tracks with origin in interval i is

$$v^i = \sum_{j=1}^M v_j^i = \sum_{j=1}^M n_j^i = n^i = \lambda_f c \Delta t^i\,, \quad \text{(A4)}$$

where Eq. (A1) is used.

The randomly oriented tracks are made observable in the light microscope by etching. Only a fraction of the tracks with a connection to the surface is revealed. The histogram of the observable tracks with various orientations is

$$\boldsymbol{e}^i = (e_1^i \dots e_j^i \dots e_M^i)^T. \quad \text{(A5)}$$

It is expected that the number of etched tracks e_j^i is proportional to their lengths:

$$\boldsymbol{e}^i = K_1(L_1 v_1^i \dots L_j v_j^i \dots L_M v_M^i)^T\,, \quad \text{(A6)}$$

where L_j is the length corresponding to the histogram column v_j^i and K_1 is a constant. Fortunately, this constant is cancelled later in the equations.

A subset of horizontal tracks $\boldsymbol{h}^i$ is selected from the etched randomly oriented tracks $\boldsymbol{e}^i$ for track length measurement:

$$\boldsymbol{h}^i = (h_1^i \dots h_j^i \dots h_M^i)^T. \quad \text{(A7)}$$

This histogram may be length biased compared to the etched tracks $\boldsymbol{e}^i$ due to track selection during measurement. Thus, the short tracks are more likely to be accepted as being horizontal than the long ones when measured in translucent light. The randomly oriented tracks v_j^i are therefore multiplied by $\varkappa_j = 1/L_j$ to compensate for this bias. Tracks measured in reflected light are not biased in this respect, therefore $\varkappa_j = 1$ in this case. See the discussion on selection bias in Jensen et al. (1992). The relation between the selected horizontal tracks and the randomly oriented tracks is therefore

$$h_j^i = K_2\, \varkappa_j\, K_1 L_j v_j^i, \quad \text{(A8)}$$

where K_2 is a constant to be cancelled later. Solving Eq. (A8) for v_j^i:

$$\frac{1}{K_2 K_1 \varkappa_j L_j} h_j^i = v_j^i \quad \text{(A9)}$$

and after summation on both sides of the equation:

$$\frac{1}{K_2 K_1} \sum_{j=1}^M \frac{h_j^i}{\varkappa_j L_j} = \sum_{j=1}^M v_j^i. \quad \text{(A10)}$$

Applying Eq. (A4) yields

$$\Delta t^i = \frac{1}{K_2 K_1 \lambda_f c} \sum_{j=1}^M \frac{h_j^i}{\varkappa_j L_j}. \quad \text{(A11)}$$

https://doi.org/10.5194/egusphere-2025-6510
Preprint. Discussion started: 13 January 2026

This equation relates the measured track length histogram $\boldsymbol{h}^i$ to the time-interval Δt^i in which the tracks were generated. In practice, this tight relationship is disturbed by crossover of tracks from nearby time intervals. It is later shown that this problem can be mediated by a mathematical technique called deconvolution. The problem with the unknown constants is solved by incorporating the surface track density in the equations.

The surface track density σ^i is related to the mean track length l^i of tracks annealed in the laboratory (Green, 1988) after generation in a short time interval Δt^i. It is assumed that the experiment mimics the natural track generation and annealing. The normalized surface track density is

$$\frac{\sigma^i}{\sigma_0^i} = f(l^i)\,, \tag{A12}$$

where l^i is the mean track length, f is an empirical relationship, and σ_0^i is the initial surface track density. It is assumed that σ_0^i is proportional to the initial track length L_0, the time Δt^i that generated the tracks, the track generation rate λ_f, and the Uranium concentration c:

$$\sigma_0^i = g\lambda_f c L_0 \Delta t^i. \tag{A13}$$

where g is the geometrical factor. Combining Eq. (A12) and (A13):

$$\sigma^i = g\lambda_f c L_0 f(l^i)\,\Delta t^i. \tag{A14}$$

The function $f(l^i)$ is valid for c-axis projected tracks (Appendix B). Inserting the expression for Δt^i, Eq. (A11), leads to the surface track density corresponding to time interval Δt^i.

$$\sigma^i = \frac{gL_0}{K_2K_1} f(l^i) \sum_{j=1}^{M} \left(\frac{h_j^i}{\varkappa_j L_j}\right). \tag{A15}$$

The total surface density σ_s caused by the track generation in all time intervals is then:

$$\sigma_s = \sum_{i=1}^{N} \sigma^i = \frac{gL_0}{K_2K_1} \sum_{i=1}^{N} \left(f(l^i) \sum_{j=1}^{M} \left(\frac{h_j^i}{\varkappa_j L_j}\right)\right). \tag{A16}$$

The ratio is

$$\frac{\sigma^i}{\sigma_s} = \frac{f(l^i) \sum_{j=1}^{M} \left(\frac{h_j^i}{\varkappa_j L_j}\right)}{\sum_{i=1}^{N} \left(f(l^i) \sum_{j=1}^{M} \left(\frac{h_j^i}{\varkappa_j L_j}\right)\right)}. \tag{A17}$$

Taking advantage of Eqs. (A14) and (A17) lead to

$$\Delta t^i = \frac{\sigma_s}{g\lambda_f c L_0} \frac{\sum_{j=1}^{M} \left(\frac{h_j^i}{\varkappa_j L_j}\right)}{\sum_{i=1}^{N} \left(f(l^i) \sum_{j=1}^{M} \left(\frac{h_j^i}{\varkappa_j L_j}\right)\right)}. \tag{A18}$$

The age of the beginning of time-interval p is obtained by summation of all time intervals from interval p to N (the most recent):

https://doi.org/10.5194/egusphere-2025-6510
Preprint. Discussion started: 13 January 2026

$$t_p = \sum_{i=p}^{N} \Delta t^i = \frac{\sigma_s}{g\lambda_f c L_0} \frac{\sum_{i=p}^{N} \sum_{j=1}^{M} \left(\frac{h_j^i}{\varkappa_j L_j}\right)}{\sum_{i=1}^{N} \left(f(l^i) \sum_{j=1}^{M} \left(\frac{h_j^i}{\varkappa_j L_j}\right)\right)}. \quad \text{(A19)}$$

The corresponding surface track density is after summation using Eq. (A17)

$$\sigma_p = \sigma_s \frac{\sum_{i=p}^{N} \left(f(l^i) \sum_{j=1}^{M} \left(\frac{h_j^i}{\varkappa_j L_j}\right)\right)}{\sum_{i=1}^{N} \left(f(l^i) \sum_{j=1}^{M} \left(\frac{h_j^i}{\varkappa_j L_j}\right)\right)}. \quad \text{(A20)}$$

$\boldsymbol{h}^i = (h_1^i \ldots h_j^i \ldots h_M^i)^T$ is the histogram of tracks generated in the time-interval Δt^i. Although most of the tracks in the elements h_j^i of length l^i are generated in the time interval Δt^i there will also be tracks from neighboring time intervals due to track length mixing. However, it was shown in Jensen and Hansen (2021) that the order can be restored, to some extent, by mathematical deconvolution. The idea is that the measured track length histogram is considered as a weighted sum of histograms of tracks generated in short time interval. These histograms, with various degrees of annealing, are derived from laboratory annealing experiments:

$$\begin{bmatrix} h^1 \\ \vdots \\ h^i \\ \vdots \\ h^M \end{bmatrix} = \hbar^1 \begin{bmatrix} g_1^1 \\ \vdots \\ g_j^1 \\ \vdots \\ g_M^1 \end{bmatrix} + \ldots \; \hbar^i \begin{bmatrix} g_1^i \\ \vdots \\ g_j^i \\ \vdots \\ g_M^i \end{bmatrix} + \ldots \; \hbar^n \begin{bmatrix} g_1^N \\ \vdots \\ g_j^n \\ \vdots \\ g_M^N \end{bmatrix} \quad \text{(A21)}$$

or

$$\begin{bmatrix} h^1 \\ \vdots \\ h^i \\ \vdots \\ h^M \end{bmatrix} = \begin{bmatrix} g_1^1 & \cdots & g_1^i & \cdots & g_1^N \\ \vdots & \vdots & \vdots & \vdots & \vdots \\ g_j^1 & \cdots & g_j^i & \cdots & g_j^N \\ \vdots & \vdots & \vdots & \vdots & \vdots \\ g_M^1 & \cdots & g_M^i & \cdots & g_M^N \end{bmatrix} \cdot \begin{bmatrix} \hbar^1 \\ \vdots \\ \hbar^i \\ \vdots \\ \hbar^N \end{bmatrix} \quad \text{(A22)}$$

or simply:

$$\boldsymbol{h} = \mathbf{G}\boldsymbol{\hbar}, \quad \text{(A23)}$$

where the vector $\boldsymbol{h}$ is the measured histogram, $\mathbf{G}$ a matrix with columns of normalized histograms derived from laboratory annealing and chosen so that their mean track length l^i is binned according with the columns of the matrix. $\boldsymbol{\hbar}$ is the vector of weights. Each histogram column in $\mathbf{G}$ is derived from neutron radiation in a short time-interval with following annealing. The columns of $\mathbf{G}$ are here based on c-axis projections of the laboratory annealed tracks described by Barbarand et al. (2003) and Ravenhurst et al. (2003). The histogram $\boldsymbol{\hbar}$ is the deconvolution of the sample histogram $\boldsymbol{h}$. In this process $\boldsymbol{h}$ is deblurred (Bardsley, 2018) with respect to track length mixing. Appendix C provides a list of various vectors and matrices.

https://doi.org/10.5194/egusphere-2025-6510
Preprint. Discussion started: 13 January 2026

The unknown $\boldsymbol{\hbar}$ in Eq. (A23) is solved using least squares probabilistic inversion (Tarantola, 2005) which includes prior information $\boldsymbol{\hbar}_{prior}$:

$$\widetilde{\boldsymbol{\hbar}} = \boldsymbol{\hbar}_{prior} + (\mathbf{G}^T\mathbf{C}_H^{-1}\mathbf{G} + \mathbf{C}_P^{-1})^{-1}\ \mathbf{G}^T\ \mathbf{C}_H^{-1}(\boldsymbol{h} - \mathbf{G}\boldsymbol{\hbar}_{prior}), \tag{A24}$$

where $\widetilde{\boldsymbol{\hbar}}$ is the posterior (the deblurred histogram) which replaces h_j^i in Eq. (A19) and (A20). $\boldsymbol{C}_H$ and $\boldsymbol{C}_P$ are data and prior variance-covariance matrixes. The least squares inversion scheme Eq. (A24) allows calculated negative posterior values in conflicts with the fact that the numbers of tracks are positive. To minimize the problem $\boldsymbol{\hbar}_{prior}$ is chosen to be with positive elements. In most cases, we do not have much information on the prior. Its elements are therefore chosen to be equal and with sum equal to the number of measured tracks. Their variances (the diagonal of $\boldsymbol{C}_P$) are chosen to be so large that all posterior tracks are allowed in a single posterior element. See Appendix D for discussion of prior values.

The variance-covariance of the deblurred histogram is calculated according to Tarantola (2005):

$$\widetilde{\mathbf{C}_P} = (\mathbf{G}^T\mathbf{C}_H^{-1}\mathbf{G} + \mathbf{C}_P^{-1})^{-1}. \tag{A25}$$

The approximation $\widetilde{\boldsymbol{h}}$ to the data histogram $\boldsymbol{h}$ is forwardly calculated based on the posterior (deblurred) histogram $\widetilde{\boldsymbol{\hbar}}$:

$$\widetilde{\boldsymbol{h}} = G\widetilde{\boldsymbol{\hbar}}\ , \tag{A26}$$

where $\widetilde{\boldsymbol{\hbar}} = (\tilde{\hbar}^1 \dots \tilde{\hbar}^i \dots \tilde{\hbar}^N)^T$.

The approximation $\widetilde{\boldsymbol{h}}^i$ to the observed tracks with origin in the time interval Δt^i is derived from Eq. (26):

$$\begin{bmatrix} g_1^1 & \dots & g_1^i & \dots & g_1^N \\ \vdots & \vdots & \vdots & \vdots & \vdots \\ \vdots & \vdots & \vdots & \vdots & \vdots \\ g_j^1 & \dots & g_j^i & \dots & g_j^N \\ \vdots & \vdots & \vdots & \vdots & \vdots \\ g_M^1 & \dots & g_M^i & \dots & g_M^N \end{bmatrix} \cdot \begin{bmatrix} 0 \\ \vdots \\ \hbar^i \\ \vdots \\ 0 \end{bmatrix} = \widetilde{\boldsymbol{h}}^i, \tag{A27}$$

where an element of $\widetilde{\boldsymbol{h}}^i$ is

$$\tilde{h}_j^i = g_j^i \hbar^i \tag{A28}$$

which replaces h_j^i in Eq. (A18) and (A19). This improves the corresponding equation given in Jensen and Hansen (2021). The final expressions for the age of the beginning of interval Δt^p is

$$t_p = \sum_{i=p}^{N} \Delta t^i = \frac{\sigma_s}{g\lambda_f c L_0} \frac{\sum_{i=p}^{N} \tilde{\hbar}^i \sum_{j=1}^{M} (\frac{g_j^i}{\varkappa_j L_j})}{\sum_{i=1}^{N} \left(f(l^i) \tilde{\hbar}^i \sum_{j=1}^{M} (\frac{g_j^i}{\varkappa_j L_j}) \right)}. \tag{A29}$$

Considering the radioactive exponential decay the final expression for the age of the oldest track in column p is obtained:

$$t_p = \frac{\eta}{\lambda_D} \ln\left(1 + \frac{\sigma_s \lambda_D}{g\lambda_f c L_0} \frac{\sum_{i=p}^{N} (\tilde{\hbar}^i \sum_{j=1}^{M} (\frac{g_j^i}{\varkappa_j L_j}))}{\sum_{i=1}^{N} \left(f(l^i) \tilde{\hbar}^i \sum_{j=1}^{M} (\frac{g_j^i}{\varkappa_j L_j}) \right)}\right), \tag{A30}$$

https://doi.org/10.5194/egusphere-2025-6510
Preprint. Discussion started: 13 January 2026

where t_p is the expected age of the oldest track in column p of the deblurred track histogram $\tilde{\boldsymbol{h}} = (\tilde{h}^1, \tilde{h}^2, \ldots \tilde{h}^i, \ldots \tilde{h}^N)^T$. The columns are counted from small to long track lengths, η is a calibration constant, λ_D is the total decay constant, σ_s is the surface track density, $g = ½$ is the geometric factor, λ_f is the U-238 fission decay constant, c is the U-238 concentration, L_0 is the mean track length of unannealed tracks, $\tilde{h}^i$ is an element of the deconvolved track length histogram, g_j^i is an element of the interpolated laboratory annealed track length histogram, $\boldsymbol{g}^i = (g_1^i \ldots g_j^i \ldots g_M^i)^T$, $\varkappa_j$ compensates for the track selection bias, $\varkappa_j = 1/L_j$ for tracks measured in transmitted light, $\varkappa_j = 1$ for tracks measured in reflected light, L_j is the track length of the tracks related to g_j^i, $f(l^i)$ is the normalized surface track density of $\tilde{h}^i$ with mean track length l^i (the track length bin of $\tilde{h}^i$ (Appendix B), N is the number of bins of the deconvolved track length histogram, M is the number of bins of the observed track length histogram.

The calibration constant η is in practice derived by calculating the oldest age using Eq. (A30) for a deconvolved unannealed track length histogram age and matching it to the apparent fission track age obtained by the usual fission track age equation. In this way we take advantage of the calibration used in the traditional age equation. The radiated sample (Barbarand et al., 2003), kept at 20 °C, is used in the calibrations.

Application of Eq. (A28) and Eq. (A20) leads to the updated expression for the surface track density

$$\sigma_p = \sigma_s \frac{\sum_{i=p}^{N}\left(f(l^i)\tilde{h}^i \sum_{j=1}^{M}\left(\frac{g_j^i}{\varkappa_j L_j}\right)\right)}{\sum_{i=1}^{N}\left(f(l^i)\tilde{h}^i \sum_{j=1}^{M}\left(\frac{g_j^i}{\varkappa_j L_j}\right)\right)}. \quad \text{(A31)}$$

Appendix B

The normalized surface track density is related to the normalized track length and described for c-axis projected tracks by Ketcham (2003). The normalized surface track density, Fig. B1, is:

$$\sigma^i/\sigma_0^i = f(l^i)\,, \quad \text{(B1)}$$

where σ^i is the observed surface track density and σ_0^i is the initial surface track density. l^i is the mean track length of observed c-axis projected tracks. The following approximation is used:

$$\frac{\sigma^i}{\sigma_0^i} = 1.0457\frac{l^i}{L_0} - 0.0457 \quad \text{for } \frac{l^i}{L_0} \geq 0.6 \text{ and} \quad \text{(B2)}$$

$$\frac{\sigma^i}{\sigma_0^i} = 0.0207\exp(5.5667\frac{l^i}{L_0}) \quad \text{for } \frac{l^i}{L_0} < 0.6. \quad \text{(B3)}$$

https://doi.org/10.5194/egusphere-2025-6510
Preprint. Discussion started: 13 January 2026

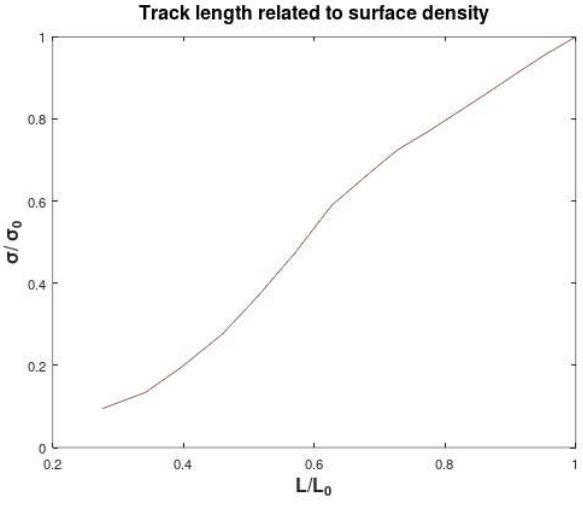

Figure B1: Reduced surface track density $\frac{\sigma^i}{\sigma_0}$ as a function of the reduced track length $\frac{l^i}{L_0}$. The track lengths are c-axis projected. The relations Eq. (B2) and (B3) are approximations to the relation shown in Ketcham (2003, Fig. 7).

Appendix C

The vectors and the matrix $\boldsymbol{G}$ are shown below to help the reader keeping track of their mutual alignments.

$$[\Delta t^1 \quad ... \quad \Delta t^i \quad ... \quad \Delta t^N\,]$$ Time intervals

$$[\sigma^1 \quad ... \quad \sigma^i \quad ... \quad \sigma^N\,]$$ Surface track densities

$$[l^1 \quad ... \quad l^i \quad ... \quad l^N\,]$$ Mean track lengths

The number of tracks $[\hbar^1 \quad ... \quad \hbar^i \quad ... \quad \hbar^N\,]$ generated in the time interval Δt^i

$$\underbrace{\begin{bmatrix} L^1 \\ \vdots \\ L^i \\ \vdots \\ L^M \end{bmatrix}}_{} \ldots\ldots \underbrace{\begin{bmatrix} h^1 \\ \vdots \\ h^i \\ \vdots \\ h^M \end{bmatrix}}_{\boldsymbol{h}} \ldots\ldots \underbrace{\begin{bmatrix} \tilde{h}^1 \\ \vdots \\ \tilde{h}^i \\ \vdots \\ \tilde{h}^M \end{bmatrix}}_{\tilde{\boldsymbol{h}}} = \underbrace{\begin{bmatrix} g_1^1 & \ldots & g_1^i & \ldots & g_1^N \\ \vdots & \vdots & \vdots & \vdots & \vdots \\ g_j^1 & \ldots & g_j^i & \ldots & g_j^N \\ \vdots & \vdots & \vdots & \vdots & \vdots \\ g_M^1 & \ldots & g_M^i & \ldots & g_M^N \end{bmatrix}}_{\boldsymbol{G}} \cdot \underbrace{\begin{bmatrix} \hbar^1 \\ \vdots \\ \hbar^i \\ \vdots \\ \hbar^N \end{bmatrix}}_{\hbar} \ldots\ldots \underbrace{\begin{bmatrix} \tilde{\hbar}^1 \\ \vdots \\ \tilde{\hbar}^i \\ \vdots \\ \tilde{\hbar}^N \end{bmatrix}}_{\tilde{\hbar}}$$

Where l^i is the track length binning, $\boldsymbol{h}$ the observed histogram (Data), $\tilde{\boldsymbol{h}}$ the forward calculated approximation to data, $\boldsymbol{G}$ the matrix of laboratory annealed tracks, $\hbar$ with elements $\hbar^i$ being the histogram of tracks generated in the time interval Δt^i, $\tilde{\hbar}$ the deconvolved track length histogram with elements $\tilde{\hbar}^i$ of tracks generated in the time interval Δt^i.

https://doi.org/10.5194/egusphere-2025-6510
Preprint. Discussion started: 13 January 2026

Appendix D

In this appendix the variance-covariance matrixes for data $\mathbf{C}_H$ and prior $\boldsymbol{C}_P$ are presented. $\mathbf{C}_H$ is defined as given in Jensen and Hansen (2021). The number of track length measurements are usually restricted to a prior fixed number e.g., one hundred. The expected variance of the number of counted tracks in each histogram column is therefore calculated as being multinomial. They are the diagonal values of the variance-covariance matrix:

$$\mathbf{C}_H(j,j) = DP_H^j(1-P_H^j) \qquad \text{for } j = 1 \dots M, \tag{D1}$$

where M is the number of bins, $P_H^j = d_{obs}^j/D$ is the probability of the observed data d_{obs}^j. D is the number of measured tracks. The covariances are off diagonal:

$$\mathbf{C}_H(l,j) = -DP_H^l P_H^j \qquad \text{for } l \neq j. \tag{D2}$$

Prior values and variances are defined so that positive posterior values (positive histogram columns) are promoted and so that restrictions on the shape of the posterior histogram are not too hard. For example, in an extreme case, it is allowed that all tracks end up in a single column. This is an improvement to the definitions given in Jensen and Hansen (2021). The probability of the default priors is $P_p^j = \frac{n_{prior}^j}{D} = \frac{D/N}{D} = 1/N$ since the priors are equally distributed over the bins. The diagonal values of the covariance-variance matrix are then

$$\mathbf{C}_p(j,j) = qDP_p^j\left(1-P_p^j\right) = D^2 \qquad \text{for } j = 1 \dots N, \tag{D3}$$

where the default factor $q = \frac{D}{N(1-\frac{1}{N})}$ is chosen to ensure room for the possibility that all posterior tracks end up in a single bin. N is the number of prior bins. The covariances are off diagonal:

$$\mathbf{C}_H(l,j) = -f^p DP_p^l P_p^j \qquad \text{for } l \neq j.$$

Code and data availability

The code and input data are available on Zenodo (Jensen, 2025a). The programming platform is Octave (Eaton et al., 2020).

Supplement

Table S1 shows calculated age nodes and figures with data from the Canadian Shield (Spiegel et al., 2023b), Zenodo (Jensen, 2025b).

Author contributions

PKJ developed the equations and the computer program. He also performed the simulations and wrote the paper.

https://doi.org/10.5194/egusphere-2025-6510
Preprint. Discussion started: 13 January 2026

Competing interests

The author has no conflicts of interest to declare.

References

Barbarand, J., Hurford, T., and Carter, A.: Variation in apatite fission-track length measurement: implications for thermal history modelling, Chem. Geol., 198, 1-2, 77-106, https://doi.org/10.1016/S0009-2541(02)00423-0, 2003.

Bardsley, J. M.: Computational uncertainty quantification for inverse problems, 19. SIAM, https://doi.org/10.1137/1.9781611975383,2018.

Bertagnolli, E., Keil, R., and Pahl, M.: Thermal history and length distribution of fission tracks in apatite, Part I., Nucl. Tracks Radiat. Meas., 7, 4, 163-177, https://doi.org/10.1016/0735-245X(83)90026-1, 1983.

Calvetti, D. and Somersalo, E.: An introduction to Bayesian scientific computing: ten lectures on subjective computing, 2, Springer Science & Business Media, https://doi.org/10.1007/978-0-387-73394-4, 2007.

Donelick, R. A.: Etchable fission track length distribution in apatite: experimental observations, theory and geological applications, Unpublished Ph.D. dissertation, Rensselaer Polytechnic Institute, Troy, New York, 414 p., 1988.

Donelick, R. A., Ketcham, R. A., and Carlson, W. D.: Variability of apatite fission-track annealing kinetics: II, Crystallographic orientation effects, Am. Min., 84, 9, 1224-1234, https://doi.org/10.2138/am-1999-0902, 1999.

Eaton, J. W., Bateman, D., Hauberg, S., and Wehbring, R.: GNU Octave version 6.1.0 manual: a high-level interactive language for numerical computations, https://www.gnu.org/software/octave/doc/v6.1.0/, 2020.

Gallagher, K.: Transdimensional inverse thermal history modeling for quantitative thermochronology, J. Geophys. Res. Solid Earth, 117, B2, http://doi.wiley.com/10.1029/2011JB008825, 2012.

Green, P. F.: The relationship between track shortening and fission track age reduction in apatite: combined influences of inherent instability, annealing anisotropy, length bias and system calibration, Earth Planet. Sci. Lett., 89, 3-4, 335-352, https://doi.org/10.1016/0012-821X(88)90121-5, 1988.

https://doi.org/10.5194/egusphere-2025-6510
Preprint. Discussion started: 13 January 2026

Jensen, P. K., Hansen, K., and Kunzendorf, H.: A numerical model for the thermal history of rocks based on confined horizontal fission tracks. International Journal of Radiation Applications and Instrumentation, Part D. Nucl. Tracks Radiat. Meas., 20, 2, 349-359, https://doi.org/10.1016/1359-0189(92)90064-3, 1992.

Jensen, P. K. and Hansen, K.: Deconvolution of fission-track length distribution, Geochronology, 3, 561–575, https://doi.org/10.5194/gchron-3-561-2021, 2021.

Jensen, P. K.: Computer code calculating fission track age nodes for c-axis projected tracks, Zenodo [code dataset]. https://doi.org/10.5281/zenodo.18062642, 2025a.

Jensen, P. K.: Age nodes for fission tracks for Ellesmere Island and Northwest Greenland, Zenodo [calculation examples], https://doi.org/10.5281/zenodo.18063819, 2025b.

Jungerman, J. and Wright, S. C.: Kinetic Energy Release in Fission of U238, U235, Th232, and Bi209 by High Energy Neutrons, Phys. Rev., 76, 1112-1116, https://doi.org/10.1103/PhysRev.76.1112, 1949.

Keil, R., Pahl, M., and Bertagnolli, E.: Thermal history and length distribution of fission tracks: Part II, International Journal of Radiation Applications and Instrumentation, Part D. Nucl. Tracks Radiat. Meas., 13, 1, 25-33, https://doi.org/10.1016/1359-0189(87)90004-5, 1987.

Ketcham, R. A.: Observations on the relationship between crystallographic orientation and biasing in apatite fission-track measurements, Am. Min., 88, 5-6, 817-829, https://doi.org/10.2138/am-2003-5-610, 2003.

Ketcham, R. A.: Forward and inverse modeling of low-temperature thermochronometry data, Rev. Mineral. Res., Geochem, 58, 1, 275-314, https://doi.org/10.2138/am-2003-5-610, 2005.

Ketcham, R. A.: Fission-Track Annealing: From Geologic Observations to Thermal History Modeling, in: Fission-Track Thermochronology and its Application to Geology, edited by: Malusà M. and Fitzgerald P, Springer Textbooks in Earth Sciences, Geography and Environment, Springer, Cham., https://doi.org/10.1007/978-3-319-89421-8_3, 2019.

Kohn, B. P., Ketcham, R. A., and Vermeesch, P. et al.: Interpreting and reporting fission-track chronological data, GSA Bulletin, February 28, https://doi.org/10.1130/B37245.1, 2024.

https://doi.org/10.5194/egusphere-2025-6510
Preprint. Discussion started: 13 January 2026

Li, W., Wang, L., Lang, M., Trautmann, C., and Ewing, R. C.: Thermal annealing mechanisms of latent fission tracks: Apatite vs. zircon, Earth Planet. Sci. Lett., 302, 1, 227-235, https://doi.org/10.1016/j.epsl.2010.12.016, 2011.

Ravenhurst, C. E., Roden-Tice, M. K., and Miller, D. S.: Thermal annealing of fission tracks in fluorapatite, chlorapatite, manganoanapatite, and Durango apatite: Experimental results, Canadian Journal of Earth Sciences. 40, 7. https://doi.org/10.1139/e03-032, 2003.

Spiegel, C., Sohi, M. S., Reiter, W., Meier, K., Ventura, B., and Lisker, F.: Phanerozoic tectonic and sedimentation history of the Arctic: Constraints from deep-time low-temperature thermochronology data of Ellesmere Island and Northwest Greenland, Tectonics, 42, https://doi.org/10.1029/2022TC007579, 2023a.

Spiegel, C., Sohi, M. S., Reiter, W., Meier, K., Ventura, B., Lisker, F., et al.: Supporting Information for Phanerozoic tectonic and sedimentation history of the Arctic: constraints from deep-time low-temperature thermochronology data of Ellesmere Island and Northwest Greenland, https://doi.org/10.5281/zenodo.8120628, 2023b.

Tarantola, A.: Inverse problem theory, SIAM, Philadelphia, https://doi.org/10.1137/1.9780898717921, 2005.